



# Turbulence characteristics within the atmospheric surface layer of the coastal region of Qatar

Yuan Li<sup>1</sup> · Reza Sadr<sup>1</sup>

Received: 28 January 2022 / Accepted: 7 April 2022 / Published online: 3 June 2022  
© The Author(s) 2022

## Abstract

The atmospheric turbulence characteristics in the coastal region of Qatar are analyzed using the measurements conducted on the shoreline (26.08 N, 51.36 E). The micrometeorological data were collected, from August 2015 to September 2016, using sonic anemometers (20 Hz) at three heights and a weather station atop a 9-m tower. The turbulence characteristics are studied within the framework of Monin–Obukhov similarity theory (MOST), in the presence of the coastal inhomogeneities generated by the sea and land surfaces coming together. The results show the wind from the north-west prevails during the entire test period, with the wind speed higher than that from other directions. The non-dimensional standard deviations of velocity components are found to be consistent the results reported around the world and match suggested MOST scaling, with a relatively greater value for the dissipation rate of turbulent kinetic energy. The flux Richardson number shows a larger scatter under the super-stable and super-unstable regimes. Moreover, the non-dimensional standard deviation of temperature does not align with the suggested model under near-neutral and very stable regimes, and the gradient Richardson number shows some negative values under stable regimes. Two different atmospheric daily stability patterns, ‘orderly’ and ‘disheveled,’ are identified based on the wind conditions. The orderly stability pattern shows a daily descending and ascending trend during the sunrise and sunset periods, respectively, while the disheveled days follow a random pattern with no clear order. The two patterns are then related to the wind continuity and direction relative to the shoreline.

**Keywords** Atmospheric boundary layer · Coastal zone · Monin–Obukhov similarity theory

## 1 Introduction

The atmospheric boundary layer (ABL) is the link between the atmosphere and the Earth’s surface that plays a vital role in the transportation of air pollutants, water vapour, and heat from the surface (Panofsky and Dutton 1984). Heat, vapour, and surface shear are efficiently transmitted within the entire ABL by the mechanism of turbulent transfer which moderates the microclimate near the ground (Arya 2001). The heat, humidity, mass, and momentum

---

✉ Reza Sadr  
reza.sadr@tamu.edu

<sup>1</sup> Department of Mechanical Engineering, Texas A&M University, College Station, TX 77843, USA

from the atmosphere are also transmitted to the surface through the same mechanism. Therefore, understanding the mixing capability of ABL turbulence is of great importance as it directly affects the speed at which harmful toxic gases released by human activities are spread throughout the lower troposphere, which to a larger extent determines the local air quality.

The ABL can be divided into stable, neutral, and unstable regimes depending on the role of forced convection and buoyancy mechanisms. In modern micrometeorology, Monin–Obukhov similarity theory (MOST) is the starting point for characterizing the state of boundary-layer stability via a universal function of the stability parameter under a steady state and horizontally homogeneous conditions (Monin and Obukhov 1954). The work of Businger et al. (1971), based on data obtained from a 1968 Kansas experiment, is widely used to characterize the universal functions for non-dimensional wind shear and thermal stratification. Kaimal and Finnigan (1994) reexamined the Kansas data and refined the similarity function through a comparison with Dyer's (1974) and Hogstrom's (1988) results. Kaimal and Finnigan (1994) further introduced three more functions to the two universal functions of Businger et al. (1971), including the non-dimensional dissipation of turbulent kinetic energy (TKE). The application of the universal function is widely discussed for different topographies in different regions of the world (Bian et al. 2003; Li et al. 2006; Dharamaraj et al. 2009); however, the assumption of homogeneity in MOST may not be applicable for terrains such as urban, forest, and coastal. For example, observations show that the non-dimensional standard deviation of horizontal velocity is sensitive to local terrain, and the non-dimensional standard deviation of temperature in the urban boundary layer does not obey MOST under stable regimes (Al-Jiboori et al. 2002). Further, Grachev et al. (2008, 2013) indicate the limitations of the universal function in the strongly stable condition of the Arctic based on the data from the Surface Heat Budget of the Arctic Ocean experiment (SHEBA).

Research on regional mesoscale circulation with different local meteorological conditions (e.g., sea breezes, slope winds, valleys, regional flows) and associated turbulence characteristics is of major relevance and has important practical applications (Garratt 1994). Of particular importance are coastal areas, which are often densely populated and contain major industries, where the dispersion of pollutants, wind power systems, marine ecology, and other human activities are affected by local ABL properties. Atmospheric boundary layers in a coastal area are typical cases of horizontal inhomogeneity due to the presence of drastically different surfaces, water, and land. Furthermore, the scale of the inhomogeneity is subject to daily and seasonal variations which must be considered for developing models of ABL in these regions.

The limited available literature on wind turbulence characteristics in coastal areas reveals unique patterns for different wind conditions at different locations, such as sea/land breezes (Novitskii et al. 2011), monsoons (Prasad et al. 2019), katabatic flow (Soloviev 2013) and shamal (Al Senafi and Anis 2015). For instance, Repina et al. (2012) observed that, in the coastal region of the Black Sea, the TKE shows substantial quasiperiodic oscillations with a period of about 3.5 h in stably stratified conditions during low and moderate winds in Ukraine. On the other hand, Cheynet et al. (2017) showed good agreement with Kaimal spectra for high wind speeds (up to  $28 \text{ m s}^{-1}$ ) at 80 m above the sea level in Germany. These observations indicate interdependence between geographical location and wind conditions, thus necessitating further investigation of atmospheric turbulence in coastal regions.

Validation of MOST in various coastal observations shows varied results. Dharamaraj et al. (2009) indicate the universal function for the normalized standard deviation of velocity components and temperature fit well with MOST in the neutrally stable conditions over the Sabarmati river basin, India. The work of Singha and Sadr (2012) provides the first coastal

boundary-layer stability study in the Middle East, using data collected from a pier 0.5 km off the coast of the Persian Gulf. Their observations of normalized, longitudinal, and transverse velocity components match well with other similarity results but with a lower normalized vertical velocity. Grachev et al. (2018) reveal that all the similarity parameters generally align with MOST, within experimental uncertainty, except for a somewhat greater scatter for normalized dissipation rate and a greater value for normalized temperature. Prasad et al.'s (2019) results show less scatter in the normalized velocity intensities for coastal India during winter than during monsoon (in summer) and fall. However, Yusup et al. (2008) show that the values for the normalized standard deviation of vertical velocity components do not adhere to MOST in coastal urban areas. Lange et al. (2004) also suggest that the MOST theory may not be valid for coastal stations under stable and warm advection. In any case, most available atmospheric stability observations are conducted for a short duration, just a few weeks to four months (Xu et al. 1997; Yusup et al. 2008; Prasad et al. 2019). Thus, more, long-term coastal atmospheric observations are needed for further MOST validation.

This work investigates the stability characteristics of the ABL on the shoreline of the Persian Gulf using high frequency data collected from three sonic anemometers mounted on a 9-m tower for a duration of 14 months. The presented results show similar seasonal trends of the Monin-Obukhov stability parameter and Richardson number as previously suggested in the literature. Two different types of daily stability pattern, not been previously recognized, are identified in this work. The two patterns, 'orderly' and 'disheveled,' are separated by the difference in the wind direction and duration. The two patterns are further investigated in terms of surface roughness and integral length scales. These two patterns show different distributions for the Obukhov stability parameter and similar distributions of the integral length scale for the coastal wind.

## 2 Experimental Site and Instrument

Measurements were conducted in the coastal region of Al Ghariyah, Qatar (26.08 N, 51.36 E), from August 2015 to September 2016 (Fig. 1). Qatar is a peninsula located on the south side of the Persian Gulf and surrounded by sea in all directions except for the Saudi Arabian border to the south. Recent climate change in the last twenty years of Qatar peninsula is described by Cheng et al. (2015). The Al Ghariyah beach is mostly covered by flat sand dunes with little grass and scrubs and a few low-level buildings located far away (+ 500 m) from the measurement site. The 9-m high tower is placed about  $40 \pm 10$  m from the sea, depending on the tide, and is mounted with three sonic anemometers (CSAT3) at heights of 3.2 m, 6.8 m, and 8.8 m. All three sonic anemometers are directly facing north and collect sonic temperatures and three-dimensional wind velocity via a CR5000 data logger. An in-home written program is used to remove spikes in the sonic data and replace them with the median value of seven points using the median filter (Brock 1986), the most versatile de-spiking choice recommended by Starckenburg et al. (2016). Flow distortion might cause a systematic error on the order of 3–5% for energy fluxes (Horst et al. 2015). However, it was established by Mauder and Zeeman (2018) that the precision of CSAT3 is very good regarding general flux measurements. Hence, the flow distortion correction is not applied in this work. A weather station (Davis Vantage Pro2) is also mounted atop the measurement tower to report wind velocity, temperature, humidity, and air pressure every 30 min. Public climate data (NOAA) from two nearby sites, Al Khor and Al Ruwais, are also used to compare

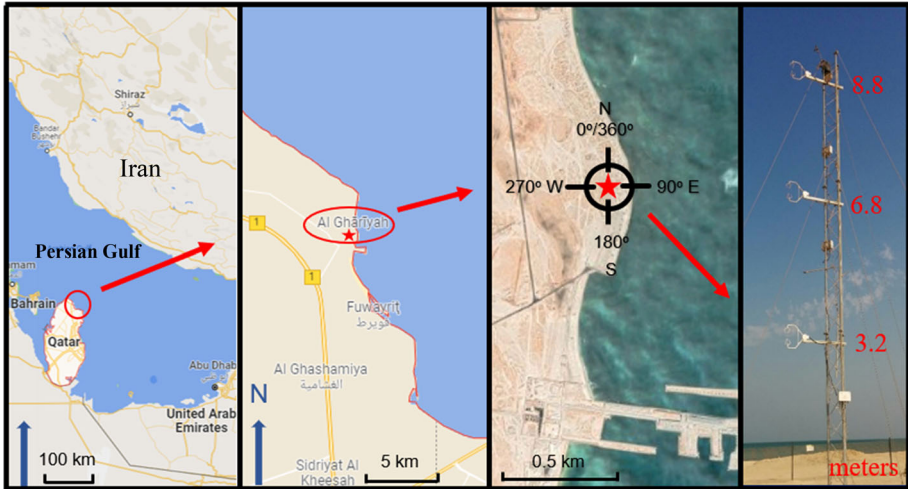


Fig. 1 Site location and view of the instrument tower

with the results in this work. It is important to note that onshore flow ( $0^\circ \text{ N} \sim 180^\circ \text{ S}$ ) is defined by the direction normal to the coastline ( $90^\circ \text{ E}$ )  $\pm 90^\circ$ .

### 3 Theoretical Background

The Monin–Obukhov stability parameter is defined as

$$\zeta = \frac{z}{L} = -\frac{z \kappa g (\overline{w'T'})}{u_*^3 T} \tag{1}$$

where  $z$  is the height above the land surface,  $L$  is the Obukhov length scale,  $\kappa = 0.4$  is the von Karman constant,  $g$  is the acceleration due to gravity,  $T$  is the sonic temperature, and  $u_* = [u'w'^2 + v'w'^2]^{1/4}$  is the friction velocity. The  $u_*$  values can also be obtained by a direct method (Sadr and Klewicki 2000) of shear stress with air density. In this work, the prime [ $x'$ ] indicates the fluctuations about the mean value for any variable  $x$ , and the overbar is an averaging operator. According to MOST, all properly scaled statistics of turbulence are universal functions of the Monin–Obukhov stability parameter. The standard deviations of velocity components  $\sigma_i$  and air temperature  $\sigma_T$  are scaled as

$$\phi_i(z/L) = \frac{\sigma_i}{u_*}, \quad i = u, v, w \tag{2}$$

$$\phi_T(z/L) = \frac{\sigma_T}{|T_*|} \tag{3}$$

where  $i(= u, v, w)$  denotes the longitudinal, transverse, and vertical velocity components, respectively, and  $T_* = -\overline{w'T'}/u_*$  is the temperature scale. To be noted,  $\phi_T$  is estimated by sonic temperature with small difference as the ‘real’  $\phi_T$ . Since Bowen ratio rarely less than 0.3 in this observation, this small difference ( $< 2\%$ ) is negligible based on the demonstration of Andreas et al. (1998). A ‘real’  $\phi_T$  can be determined with a correction based on the sonic

temperature and specific humidity (Schotanus et al. 1983; Liu et al. 2001). Similarly, the normalized vertical gradients of the mean wind speed ( $\bar{u}$ ) and temperature may be defined as

$$\phi_m = (\kappa z/u_*) (\partial \bar{u} / \partial z), \quad (4)$$

$$\phi_h = (\kappa z/T_*) (\partial \bar{T} / \partial z). \quad (5)$$

The normalized TKE dissipation rate  $\varepsilon$  in the MOST framework is expressed as

$$\phi_\varepsilon = \frac{\kappa z \varepsilon}{u_*^3}. \quad (6)$$

The dissipation rate of TKE is estimated from

$$\varepsilon = \frac{2\pi}{\bar{u}} \left[ \frac{S_u(f) f^{5/3}}{\alpha} \right]^{3/2}, \quad (7)$$

where  $S_u(f)$  is the power spectral density,  $f$  is the frequency, and  $\alpha = 0.55$  is the Kolmogorov constant.

Moreover, Richardson numbers are obtained from the velocity and temperature profile gradient within the boundary layer to assess its dynamic stability parameter. The gradient Richardson number is defined as

$$R_i = \left( \frac{g}{T} \right) \frac{dT/dz}{(\partial \bar{u} / \partial z)^2} = \left( \frac{z}{L} \right) \left( \frac{\phi_h}{\phi_m^2} \right) \quad (8)$$

The flux Richardson number ( $R_f$ ) is defined as the ratio of the buoyancy contribution to wind shear:

$$R_f = - \left( \frac{g}{T} \right) \frac{\overline{w'T'}}{u_*^2 (\partial \bar{u} / \partial z)} = \left( \frac{z}{L} \right) \frac{1}{\phi_m}. \quad (10)$$

## 4 Results and Discussion

Among the 14 months of observations, data for 12 months are studied as a one-year test period, from September 2015 to August 2016. The data show that 66% of the flow at this site is offshore ( $180^\circ < \text{direction} < 360^\circ$ ), with the wind from the north-west prevailing over other directions. The average wind speed is  $4.7 \text{ m s}^{-1}$ , and the highest wind velocity is  $14.3 \text{ m s}^{-1}$ , with a diurnal averaged temperature and relative humidity of  $26^\circ \text{C}$  and 70%, respectively. Detailed annual climate patterns and statistics for seasonal winds, temperature, humidity, and air pressure for this site are discussed by Li and Sadr (2021).

Figure 2 shows seasonal effects on the ABL stability in terms of the classical MOST universal function for thermally and aerodynamically inhomogeneous surfaces, where the error bar for spring data is presented as a typical 95% confidence level for the collected data. The normalized variances of wind components maintain similar patterns for all seasons, where  $\phi_w$  is very similar for all seasons and  $\phi_{u,v}$  varies relatively more. However, the differences between seasons are within the margin of error and small enough to be neglected. Figure 2 also compares the results of this study with the suggested trends over similar landscapes in urban China (Xu et al. 1997; Al-Jiboori et al. 2002) and coastal Malaysia (Yusup et al. 2008). The data in this figure show a slightly higher trend than that of Al-Jiboori et al. for  $\phi_u$  and  $\phi_v$  and a lower trend than that of Xu et al., but all trends remain within the standard deviations

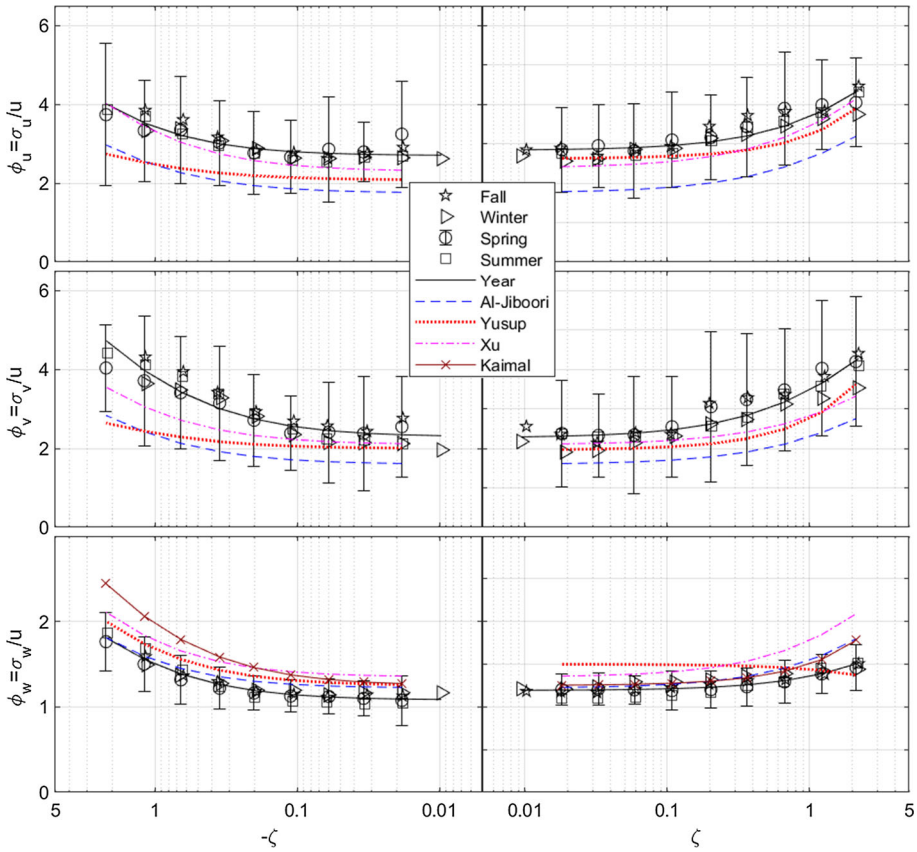


**Fig. 2** Non-dimensional standard deviation of three velocity components for the top sonic anemometer during September 2015–August 2016

of the data. The results of Yusup et al. show a descending trend in stable conditions which is associated with the low buoyancy and high frictional forces for their dataset. The trends of  $\phi_w$  in the presented data are in agreement with the predictions of Kaimal and Finnigan (1994), especially under stable condition ( $\zeta > 0$ ). There has been a debate in the literature if  $\phi_u$  and  $\phi_v$  should obey MOST predictions under different canopy and terrain conditions, where larger scatter data are found in  $\phi_u$  and  $\phi_v$  than  $\phi_w$  under this observation (Panofsky et al. 1977, Banerjee et al. 2015). Meanwhile, the differences among the observational trends for  $\phi_u$  and  $\phi_v$  of various sites are also relatively larger. However, the presented data for  $\phi_{u,v,w}$  are similar to other reported MOST prediction trends for coastal regions (Dharamaraj et al. 2009; Prasad et al. 2019).

Results of Hare et al. (1997), Mahrt et al. (1998) show that the calculated atmospheric stability parameters may behave differently if measured too close to the ground (~ 2.5 m) due to variations in the vertical structure of the atmosphere. During the Risø Air Sea Experiment (RASEX), the wind field at the 3-m level exhibited some coherence with the sea surface wave field, but such coherence was not exhibited at the 6- and 10-m levels. Grachev et al. (2018) also reported that the universal function  $\phi_{u,w}$  shows a greater scatter for the lower level (2.0 m) of the shore tower than at the higher level (5.9 m). Figure 3 shows the variations



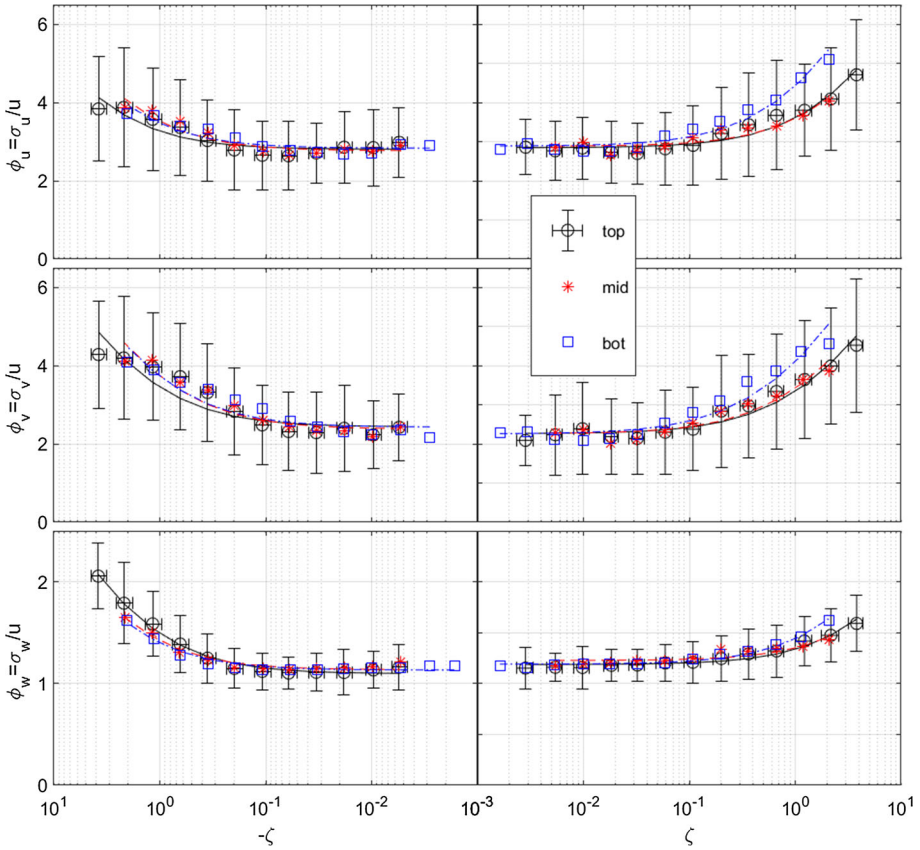


**Fig. 3** Non-dimensional standard deviations of three velocity components during September 2015–August 2016, collected from top, middle, and bottom sonic anemometers (8.8, 6.8, and 3.2 mm, respectively)

in  $\sigma_i/u_*$  ( $i = u, v, w$ ) for the three different measurement heights of 3.2 m 6.8 m and 6.8 m for the duration of the test campaign. This figure shows that the  $\phi_u$ ,  $\phi_v$ , and  $\phi_w$  are well within the standard deviation of data for all three heights, especially for  $\phi_w$ . At the 3.2 m level a larger value for  $\phi_u$  and  $\phi_v$  is observed in stable conditions, which may be related to the closer proximity to the internal boundary layer (Garratt 1994), a characteristic of the coastal terrain caused by the step change and discontinuity in surface properties and surface roughness.

The normalized standard deviation of the sonic temperature  $\phi_T$  as a function of  $\zeta$  is shown in Fig. 4 where the solid lines correspond to  $\phi_T = 2(1 - 9.5\zeta)^{-1/3}$  for  $\zeta < 0$  and  $\phi_T = 2(1 + 0.5\zeta)^{-1}$  for  $\zeta > 0$  (Kaimal and Finnigan 1994). This figure shows a higher scatter than those of the normalized velocity components. The measurements align with the suggested correlation by Kaimal, except for the near-neutral and very stable regimes where the data systematically sit above the suggested curve. Meanwhile,  $\phi_T$  shows a lower scatter in the middle range of  $0.01 < |\zeta| < 1$ . However, as  $|\zeta|$  reaches to zero, the behaviour of  $\phi_T$  is ambiguous because the temperature scale is small and trends to zero. This behaviour is consistent with the results of Grachev et al. (2018, 2021) for a coastal zone in North Carolina and Ferryland.

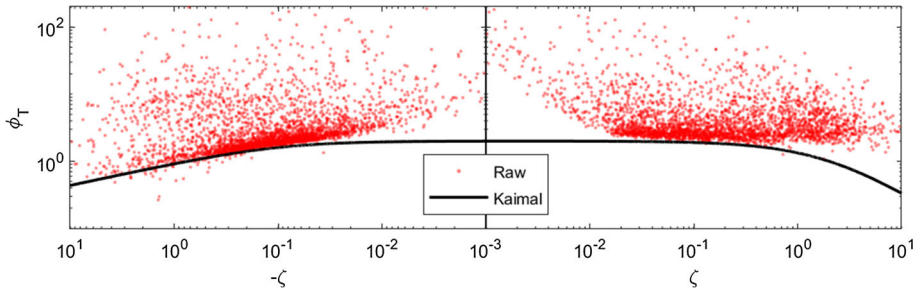


**Fig. 4** Normalized standard deviation of the sonic temperature  $\phi_T$  for the top sonic anemometer during September 2015–August 2016

The normalized dissipation rate of TKE  $\phi_\epsilon$  versus  $\zeta$  is shown in Fig. 5. Data deviating by more than 20% from the theoretical  $-5/3$  slope within the inertial subrange are excluded from the analysis (Grachev et al. 2018, 2021). The solid lines correspond to  $\phi_\epsilon = (1 + 0.5|\zeta|^{2/3})^{3/2}$  for  $\zeta < 0$  and  $\phi_\epsilon = 1 + 5\zeta$  for  $\zeta > 0$  (Kaimal and Finnigan 1994). Figure 5 shows a good agreement between trends in the presented data and the suggested Kaimal function (solid line), but for a relatively greater value of the  $\phi_\epsilon$ .

In addition,  $R_f$  and  $R_i$  are obtained using a second-order polynomial to evaluate the derivative with respect to  $z$  for the three different measurements. Figure 6a and b shows the flux Richardson number  $R_f$  vs.  $\zeta$  for this measurement campaign in comparison with the suggested correlations  $R_f = \zeta(1 - 16\zeta)^{1/4}$  for  $\zeta < 0$  and  $R_f = \zeta(1 + 5\zeta)^{-1}$  for  $\zeta > 0$  (Kaimal and Finnigan 1994). Overall, our data fit well with the suggested correlations with a larger scatter for the extremely stable and extremely unstable regimes. Figure 6c and d shows that the trends of the gradient Richardson number  $R_i$  basically correspond with the suggested trend by Kaimal and Finnigan (1994),  $R_i = \zeta$  for  $\zeta < 0$  and  $R_f = \zeta(1 + 5\zeta)^{-1}$  for  $\zeta > 0$ . The sign of  $R_i$  aligns with the sign of  $\phi_h$  for  $\zeta > 0$  based on Eq. 8. Negative values of  $R_i$  for  $\zeta > 0$  are a consequence of a negative temperature gradient that implies the vertical components of the turbulent fluxes are counter to the mean temperature gradients. A negative  $\phi_h$  is also reported by Grachev et al. (2018) for  $\zeta > 0$ , associated with negative temperature gradients. A comparison of Figs. 9 and 10 confirms that the flux–variance similarity shows better agreement with the suggested trend for MOST than the flux–gradient similarity (Rannik 1998; Nadeau et al. 2013).

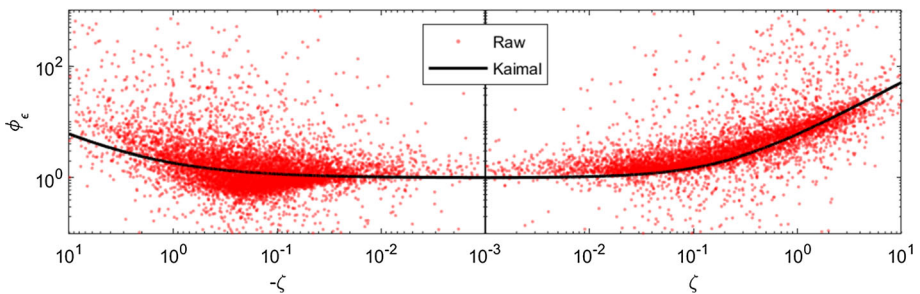


**Fig. 5** Normalized dissipation rate of TKE  $\phi_\epsilon$  for the top sonic anemometer during September 2015–August 2016



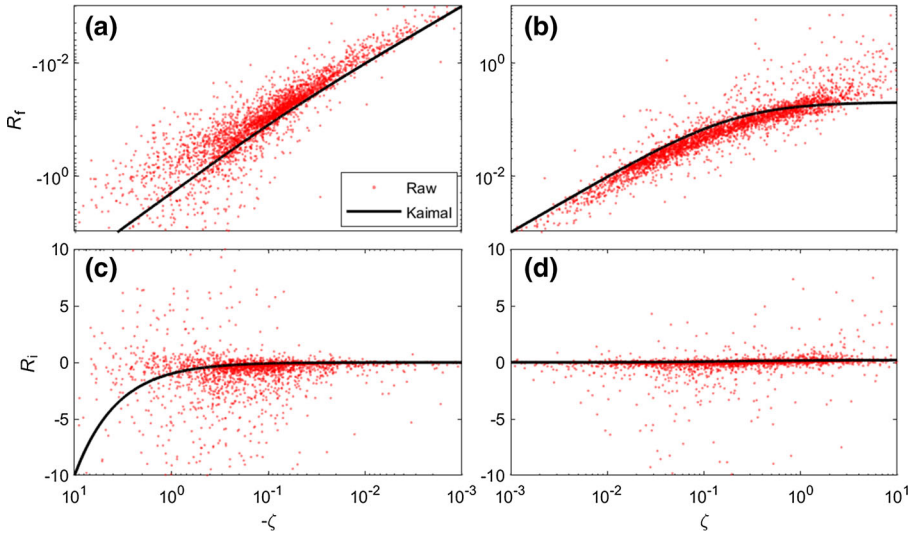


**Fig. 6** Flux and gradient Richardson number versus  $\zeta$  during September 2015–August 2016

Trends of  $\phi_{u,v,w}$  versus  $\zeta$  are affected by self-correlation because of the appearance of  $u_*$  in both definitions  $\phi_{u,v,w}$  and  $\zeta$ , Eqs. 1 and 2. The function  $\phi_m \phi_w^{-1} = \left(\frac{\kappa z}{\sigma_w}\right) \frac{dU}{dz}$  may be used to test the sensitivity of the results to self-correlation (Grachev et al. 2018) since  $u_*$  is canceled in this function. Figure 7 shows values of  $\phi_m \phi_w^{-1}$  as a function of  $\zeta$  where the solid lines correspond to  $\phi_m \phi_w^{-1} = 0.8(1 - 16\zeta)^{-1/4}(1 - 3\zeta)^{-1/3}$  for  $\zeta < 0$  and  $\phi_m \phi_w^{-1} = 0.8(1 + 5\zeta)(1 + 0.2\zeta)^{-1}$  for  $\zeta > 0$  (Kaimal and Finnigan 1994). The scatter around the suggested curve does not change substantially for most of the range of  $\zeta$  studied in this work, except for the low negative range of  $\zeta < -10^{-2}$ . This indicates that the self-correlation would likely not affect our overall results except at the low negative  $\zeta$  which corresponds to the larger scatter in super-unstable regions (Fig. 2). The change in the scatter of the data in this plot is similar to the trend reported by Grachev et al. (2018).

The results presented above provide a general comparison of ABL stability criteria in the coastal region of Qatar with the general theory of stability and other published works for the coastal region. The daily stability patterns for the duration of the measurement campaign are

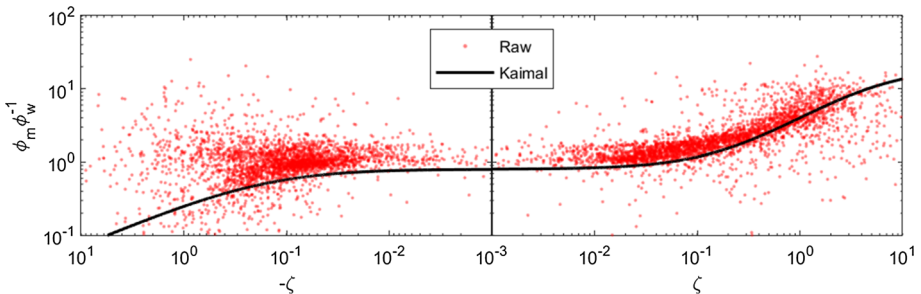


**Fig. 7** Function  $\phi_m \phi_w^{-1}$  calculated at  $z = 8.8$  m during September 2015–August 2016

further investigated using averaged values for 30-min increments. Figure 8 shows the ABL stability patterns from two sample days, where the shaded gray parts indicate the time ranges for sunrise and sunset during the year in local time, UTC + 3 h. Considering the large scatter and scarce data from  $|\zeta| > 2$ , the stability range as indicated in Table 1 is considered in this work (Sorbján and Grachev 2010; Rodrigo et al. 2015). The stability characteristics of the ABL in Fig. 8a shows it is mostly unstable during the day and stable at night, as is typically reported in the literature for other sites and terrains. During these “orderly days,” the stability parameter shows a descending trend during sunrise and an ascending trend during sunset, with enough time for the state to shift between stable and unstable in near-neutral conditions. This near-neutral condition is also indicated by the large magnitude of the Obukhov length. However, for “disheveled days,” as shown in Fig. 8b, both unstable and stable regions during day and night are observed but not in an orderly fashion, and there is no clear near-neutral pattern during sunrise and sunset. For these days, the stability fluctuates chaotically during both day and night with more time in unstable regimes.

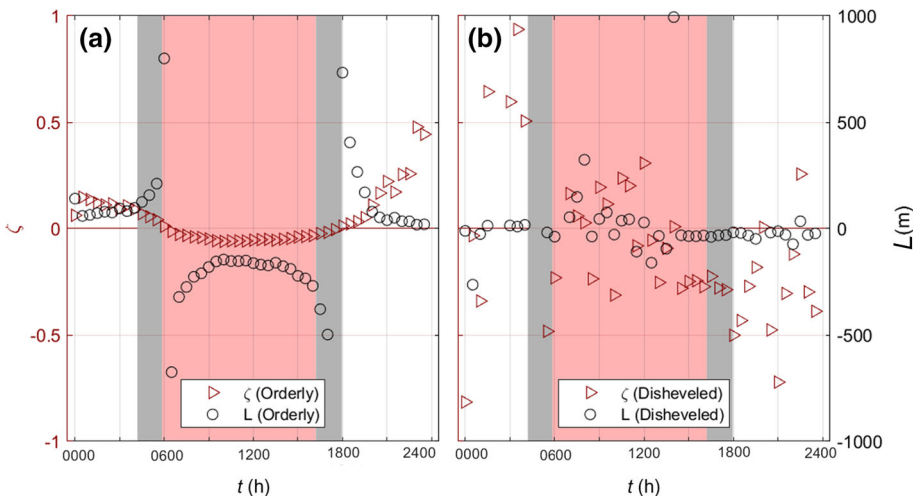


**Fig. 8** Two daily variations in the stability parameter  $\zeta$  and Obukhov length  $L$

**Table 1** Stability classification

	Current work
Extremely stable	$\zeta > 2$
Very stable	$0.6 < \zeta < 2$
Weakly stable	$0.02 < \zeta < 0.6$
Nearly neutral	$-0.02 < \zeta < 0.02$
Weakly unstable	$-0.02 < \zeta < -0.6$
Very unstable	$-2 < \zeta < -0.6$
Extremely unstable	$\zeta < -2$

The 30-min averaged data for the duration of the measurement campaign were further analyzed to better understand different trends observed and identify a possible relationship between stability and wind. The three wind parameters that are considered are speed, direction, and duration. By comparing the variations in the stability index  $\zeta$  with the three mentioned parameters, it is found that the two daily stability patterns can be categorized under two different wind direction zones and continuity durations as: (a) the orderly days when the duration of onshore flow is less than 10%; (b) the disheveled day when the duration of onshore flow is more than 10% of the time.

It should be noted we excluded days that did not have 100% of the 24 h data available for analysis. Technically, an ‘orderly’ day is a day when flow is onshore ( $0^\circ \sim 180^\circ$ ) for a maximum duration of 2 h in a day. A disheveled day is when flow is onshore for a minimum duration of 2 h in a day. Figure 9 presents the data for the two months of data, with (a) and (b) for ‘orderly’ days, and (c) and (d) for ‘disheveled’ days. Figure 9b shows a clear, smooth trend for each ‘orderly’ day with a similar trend as those shown in Fig. 8a, whereas Fig. 9d shows ‘disheveled’ days with similar patterns to that of Fig. 8b. It is important to emphasize that in addition to ‘disheveled’ days not showing a clear, daily stability pattern, no correlation with wind direction is observed. While similar trends occur throughout the test period, Fig. 9 only shows the data for 43 days, during June and July, for clarity.

Figure 10 shows the probability for the wind direction and stability parameter  $\zeta$  for the whole test period where there are 86 ‘orderly’ days and 120 ‘disheveled’ days identified. It is interesting to note that there are fewer ‘orderly’ days than ‘disheveled’ days, even though the wind coming from the sea ( $0^\circ \sim 180^\circ$ ) makes up the smaller portion of the overall data (Fig. 10a). Hence, for the wind in the identified direction, duration also plays a vital role for ‘orderly’ days. The wind during the ‘orderly’ days shows an almost normal distribution with its peak at  $315^\circ$  from the north-west (over the land), while the wind direction in the ‘disheveled’ days is almost uniformly distributed in all directions, with slightly more

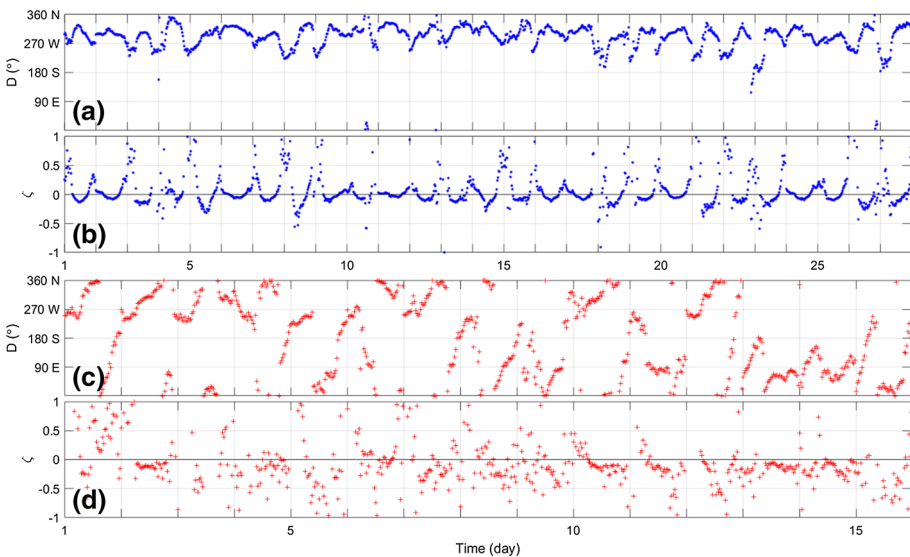


**Fig. 9** Wind directions and stability parameter  $\zeta$  (a and b) for ‘orderly’ days and (c and d) for ‘disheveled’ days in June and July 2016

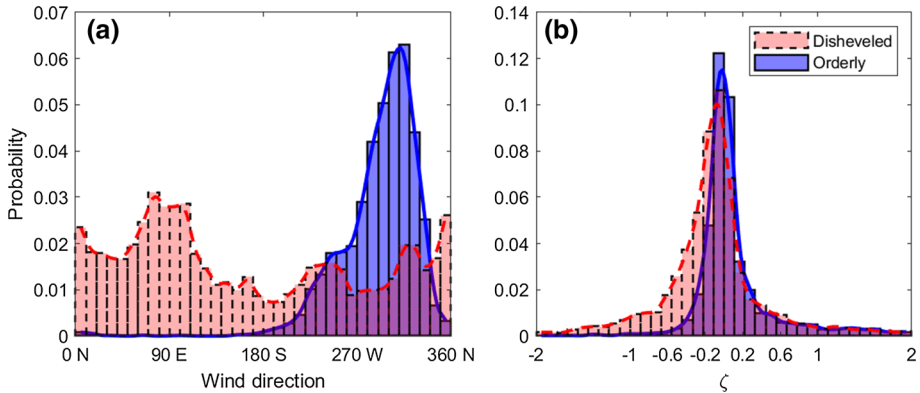


**Fig. 10** Probability distribution of (a) wind direction and (b) stability parameter for September 2015–August 2016

occurrences of short winds from the east (the sea). The probability distribution of the stability parameter  $\zeta$  in Fig. 10b shows a narrower distribution for the ‘orderly’ days, containing fewer unstable periods than that of the ‘disheveled’ days as previously discussed.

The chaotic behavior of the disheveled pattern could be caused by the inhomogeneity of the roughness between the land and the sea. The terrain roughness length ( $z_0$ ) for the TBL in this measurement campaign may be estimated under near-neutral conditions ( $|z/L| < 0.02$ ). The velocity measurement of the three sonic anemometers at different heights is used to obtain the surface roughness (Arya 2001) for disheveled and orderly days. The roughness length for the wind coming from land is  $z_{0\_Land} = (2.63 \pm 1.36) \times 10^{-2}$  while the roughness length for the wind coming from sea is  $z_{0\_Sea} = (5.74 \pm 4.27) \times 10^{-5}$ , where the numbers after the ‘ $\pm$ ’ indicate the standard deviation. It is observed that  $z_{0\_Land}$  is almost three orders of magnitude larger than  $z_{0\_Sea}$ . This significant inhomogeneity of roughness between the wind from the land and the sea is believed to be a reason for the disheveled stability pattern in Fig. 8b.

Turbulence length scales under the two stability patterns may be used to clarify if the chaotic stability pattern of the disheveled flow is caused by the local thermally forced flow dominated by gustiness or if it is independent of the wind scale. The integral length scales ( $L_{uu}$ ), which usually identify the largest eddy in a flow, are introduced to quantify the structure of the layering of the flow. Figure 11 shows calculated  $L_{uu}$  at the three measurement heights ( $z$ ) using the velocity autocorrelation method (Moore et al. 1985; Wei et al. 2014; Stull 1988). Figure 11 indicates that integral length scale profiles for the wind from the land and the sea are within the same order of magnitude at all three measurement heights. Hence, large-, medium-, and small-scale winds exist in the wind from the sea just as with the wind from the land. This figure basically shows that the wind flowing from land or sea, during the day and night, contains similar eddy sizes and is not much different in terms of gustiness. As expected, Fig. 11 shows that  $L_{uu}$  increases with the height from the ground, which implies that the turbulence has smaller eddy sizes closer to the ground. Figure 12 shows the probability distribution of  $L_{uu}$  (at all levels) for orderly and disheveled days in the whole measurement campaign. This figure shows that both the orderly and disheveled days show similar distribution with an integral length scale mean of around 40 m. Interestingly,  $L_{uu}$  is slightly larger during the disheveled days than that in orderly days, even though the offshore flow has a higher speed than that from the sea (Li and Sadr 2021).

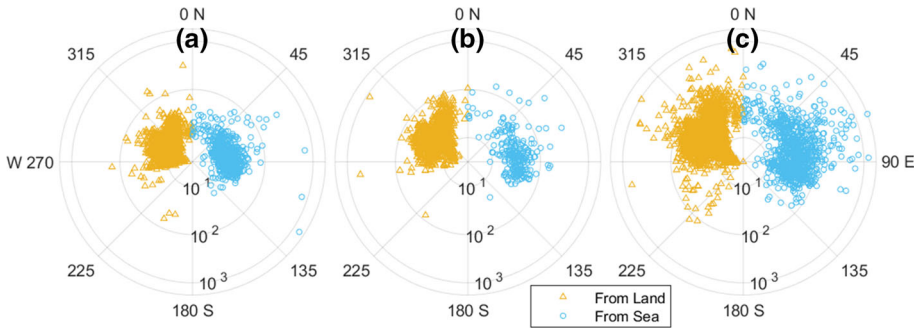


**Fig. 11** Integral length scale for the (a) bottom, (b) middle, and (c) top level for September 2015–August 2016

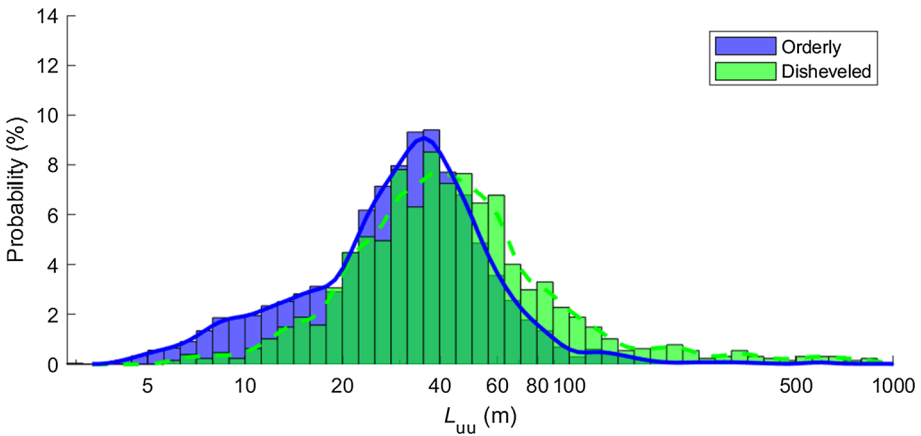


**Fig. 12** Probability of the integral length scale for September 2015–August 2016

### 5 Summary

Atmospheric-surface-layer stability is studied in the coastal region of Qatar (Al Ghariyah 26.08 N, 51.36 E) from September 2015 to August 2016. Turbulence data were collected at three heights from the ground–3.2 m, 6.8 m, 8.8 m—through three sonic anemometers placed on the 9-m observational tower, and the mean meteorological data were collected at the top. The results show a yearly average wind speed of 4.7 m s<sup>-1</sup>, mostly from the north-west, with a diurnal average temperature and relative humidity of 26 °C and 70%, respectively.

The universal relationship for the normalized turbulence statistics as a function of the local Monin–Obukhov stability parameter  $\zeta$  is studied. The universal functions for non-dimensional standard deviation  $\phi_w$  versus stability parameter  $\zeta$  generally follow the Monin–Obukhov similarity theory for all stability conditions, heights, and seasons, within experimental uncertainty. However, variations in normalized standard deviation  $\phi_T$  with  $\zeta$  do not align well with predictions for near-neutral and very stable regimes and are systematically above the curve suggested by Kaimal and Finnigan (1994). The trends for normalized dissipation rate of TKE  $\phi_\epsilon$  with  $\zeta$  show good agreement with the suggested Kaimal function but with relatively elevated values. The trend for the flux Richardson number  $R_f$  as a function of  $\zeta$  aligns well

with the trend suggested by Kaimal and Finnigan (1994) but indicates a larger scatter under the super-stable and unstable regimes. The variations in gradient Richardson number  $R_i$  with  $\zeta$  mostly follow the suggested trends in the literature, but some negative values of  $R_i$  are observed in the stable regime.

Diurnal stability data are further investigated to identify the effect of wind patterns on the stability status of the ABL at this coastal site. Two different stability trends, ‘orderly’ and ‘disheveled,’ are identified at this location and correlated with wind direction and duration. The clear pattern for the near-neutral condition during the sunrise and sunset is detected in ‘orderly’ days and a chaotic random pattern for ‘disheveled’ days. The probability distribution of the stability parameter  $\zeta$  shows a narrower distribution for the ‘orderly’ days, containing fewer unstable periods than the ‘disheveled’ days. The chaotic trend during disheveled days could be caused by the inhomogeneity of the roughness between the land and the sea (1000 times). Flow from the land and the sea is within the same length scale. During the disheveled days, the  $L_{uu}$  is slightly larger than that in orderly days. Hence, the daily pattern for the orderly and disheveled days is independent of the integral length scales.

**Acknowledgements** The authors would like to greatly acknowledge the financial support provided by the Qatar National Research Fund (QNRF) through its research Grant (NPRP ID: 05-543-2-220) and thank TAMUQ machine shop personnel for assisting in setting up the tower. We are grateful to Qatar Museum Authority for granting access to the site.

**Funding** Open Access funding provided by the Qatar National Library.

**Data availability** The datasets generated during and/or analyzed during the current study are available from the corresponding author on reasonable request.

**Open Access** This article is licensed under a Creative Commons Attribution 4.0 International License, which permits use, sharing, adaptation, distribution and reproduction in any medium or format, as long as you give appropriate credit to the original author(s) and the source, provide a link to the Creative Commons licence, and indicate if changes were made. The images or other third party material in this article are included in the article’s Creative Commons licence, unless indicated otherwise in a credit line to the material. If material is not included in the article’s Creative Commons licence and your intended use is not permitted by statutory regulation or exceeds the permitted use, you will need to obtain permission directly from the copyright holder. To view a copy of this licence, visit <http://creativecommons.org/licenses/by/4.0/>.

## References

- Al-Jiboori MH, Xu Y, Qian Y (2002) Local similarity relationships in the urban boundary layer. *Boundary-Layer Meteorol* 102:63–82
- Al Senafi F, Anis A (2015) Shamals and climate variability in the Northern Arabian/Persian Gulf from 1973 to 2012. *Int J Climatol* 35:4509–4528
- Andreas EL, Hill RJ, Gosz JR, Moore DI, Otto WD, Sarma AD (1998) Statistics of surface-Layer turbulence over terrain with metre-scale heterogeneity. *Boundary-Layer Meteorol* 86:379–408
- Arya S (2001) Introduction to micrometeorology. Academic Press, San Diego
- Banerjee T, Katul GG, Salesky ST, Chamecki M (2015) Revisiting the formulations for the longitudinal velocity variance in the unstable atmospheric surface layer. *Q J R Meteorol Soc* 141(690):1699–1711
- Bian L, Xu X, Lu L, Gao Z, Zhou M, Liu H (2003) Analysis of turbulence parameters in the near surface layer at Qamdo of the Southeastern Tibetan Plateau. *Adv Atmos Sci* 20(3):369–378
- Brock F (1986) A nonlinear filter to remove impulse noise from meteorological data. *J Atmos Oceanic Tech* 3(1):51–58
- Businger JA, Wyngaard JC, Izumi Y, Bradley E (1971) Flux-profile relationships in the atmospheric surface layer. *J Atmos Sci* 28(2):181–189
- Cheng WL, Saleem A, Sadr R (2015) Recent warming trend in the coastal region of Qatar. *Theoret Appl Climatol* 128:193–205



- Cheyne E, Jakobsen JB, Obhrai C. (2017). Spectral characteristics of surface-layer turbulence in the North Sea. *Energy Procedia*. Elsevier Ltd, 414–427.
- Dharamaraj T, Chintalu GR, Raj PE (2009) Turbulence characteristics in the atmospheric surface layer during summer monsoon of 1997 over a semi-arid location in India. *Meteorol Atmos Phys* 104:113–123
- Dyer A (1974) A review of flux-profile relationships. *Bound-Layer Meteorol* 7(3):363–372
- Garratt JR (1990) The internal boundary layer—a review. *Boundary-Layer Meteorol* 50:171–203
- Garratt JR (1994) Review: the atmospheric boundary layer. *Earth-Sci Rev* 37(1–2):89–134
- Golder D (1972) Relations among stability parameters in the surface layer. *Boundary-Layer Meteorol* 3(1):47–58
- Grachev A, Andreas E, Fairall C, Guest P, Persson P (2008) Turbulent measurements in the stable atmospheric boundary layer during SHEBA: ten years after. *Acta Geophys* 56(1):142–166
- Grachev AA, Andreas EL, Fairall CW, Guest PS, Persson POG (2013) The critical richardson number and limits of applicability of local similarity theory in the stable boundary layer. *Bound-Layer Meteorol* 147(1):51–82
- Grachev AA, Leo LS, Fernando HJS, Fairall CW, Creegan E, Blomquist BW, Christman AJ, Hocut CM (2018) Air–Sea/Land Interaction in the Coastal Zone. *Bound-Layer Meteorol*. 167(2):181–210
- Grachev AA, Krishnamurthy R, Fernando HJS et al (2021) Atmospheric turbulence measurements at a coastal zone with and without fog. *Boundary-Layer Meteorol* 181:395–422
- Hare JE, Hara T, Edson JB, Wilczak JM (1997) A similarity analysis of the structure of airflow over surface waves. *J Phys Oceanogr* 27:1018–1037
- Hogstrom U (1988) Non-dimensional wind and temperature profiles in the atmospheric surface layer: a re-evaluation. *Bound-Layer Meteorol* 42(1–2):55–78
- Horst TW, Semmer SR, Maclean G (2015) Correction of a non-orthogonal, three-component sonic anemometer for flow distortion by transducer shadowing. *Boundary-Layer Meteorol* 155:371–395
- Kaimal JC, Finnigan JJ (1994) Atmospheric boundary layer flows: their structure and measurements. Oxford University Press, Oxford
- Lange B, Larsen S, Højstrup J, Barthelmie R (2004) The influence of thermal effects on the wind speed profile of the coastal marine boundary layer. *Bound Layer Meteorol* 112(3):587–617
- Li M, Ma Y, Ma W, Hu Z, Ishikawa H, Zhongbo Su, Sun F (2006) Analysis of turbulence characteristics over the northern Tibetan plateau area. *Adv Atmos Sci* 23(4):579–585
- Li Y, Sadr R (2021) Diurnal wind pattern and climate condition on the coastal region of Qatar. *J Sci Res Rep* 27(1):37–51
- Liu HP, Peters G, Foken T (2001) New equations for sonic temperature variance and buoyancy heat flux with an omnidirectional sonic anemometer. *Boundary-Layer Meteorol* 100(3):459–468
- Mahrt L, Vickers D, Edson J, Sun J, Højstrup J, Hare J, Wilczak JM (1998) Heat flux in the coastal zone. *Boundary-Layer Meteorol* 86(3):421–446
- Mauder M, Zeeman MJ (2018) Field intercomparison of prevailing sonic anemometers. *Atmos Meas Tech* 11:249–263
- Monin A, Obukhov A (1954) Basic laws of turbulent mixing in the surface layer of the atmosphere. *Contrib Geophys Inst Acad Sci USSR* 24(151):163–187
- Moore GE, Liu MK, Shi LH (1985) Estimates of integral time scales from a 100-m meteorological tower at a plains site. *Boundary Layer Meteorol* 31:349–368
- Nadeau DF, Pardyjak ER, Higgins CW, Parlange MB (2013) Similarity scaling over a steep alpine slope. *Boundary-Layer Meteorol* 147(3):401–419
- Novitskii MA, Gaitandzhiev DE, Mazurin NF, Matskevich MK (2011) Turbulence characteristics in the coastal zone with breeze circulation. *Russ Meteorol Hydrol* 36(9):580–589
- Panofsky HA, Tennekes H, Lenschow DH et al (1977) The characteristics of turbulent velocity components in the surface layer under convective conditions. *Boundary-Layer Meteorol* 11:355–361
- Panofsky H, Dutton J (1984) Atmospheric turbulence: models and methods for engineering applications. Wiley, New York, p 397
- Prasad KBRRH, Srinivas CV, Singh AB, Naidu CV, Baskaran R, Venkatraman B (2019) Turbulence characteristics of surface boundary layer over the Kalpakkam tropical coastal station, India. *Meteorol Atmos Phys Springer Wien* 131(4):827–843
- Rannik Ü (1998) On the surface layer similarity at a complex forest site. *J Geophys Res* 103(D8):8685–8697
- Repina I, Artamonov A, Chukharev A, Esau I, Goryachkin Y, Kuzmin A, Pospelov M, Sadovsky I, Smirnov M (2012) Air–sea interaction under low and moderate winds in the Black Sea coastal zone. *Estonian J Eng*. 18(2):89
- Rodrigo JS, Cantero E, García B, Borbón F, Irigoyen U, Lozano S, Fernande PM, Chávez RA (2015) Atmospheric stability assessment for the characterization of offshore wind conditions. *J Phys Conf Ser* 625:012044

- Sadr R, Klewicki J (2000) Surface shear stress measurement system for boundary layer flow over a salt playa. *Meas Sci Technol* 11:1403–1413
- Schotanus P, Nieuwstadt FTM, De Bruin HAR (1983) Temperature measurement with a sonic anemometer and its application to heat and moisture fluxes. *Boundary-Layer Meteorol* 26:81–93
- Singha A, Sadr R (2012) Characteristics of surface layer turbulence in coastal area of Qatar. *Environ Fluid Mech* 12(6):515–531
- Soloviev YP (2013) Measurements of the atmospheric turbulence in the coastal zone of the sea during weak wind from a mountainous coast. *Izvestiya Atmos Ocean Phys* 49(3):315–328
- Sorbjan Z, Grachev AA (2010) An evaluation of the flux-gradient relationship in the stable. *Boundary-Layer Meteorol* 135:358–405
- Starkenburg D, Metzger S, Fochesatto GJ, Alfieri JG, Gens R, Prakash A, Cristóbal J (2016) Assessment of despiking methods for turbulence data in micrometeorology. *J Atmos Oceanic Tech* 33(9):2001–2013
- Stull RB (1988) An introduction to boundary layer meteorology. Kluwer Academic Publishers, Dordrecht
- Wei X, Dupont E, Gilbert E, Musson-Genon L, Carissimo B (2014) A preliminary analysis of measurements from a near-field pollutants dispersion campaign in a stratified surface layer. *Int J Environ Pollut* 55:183–191
- Xu Y, Zhao C, Li Z, Wei Z (1997) Turbulent structure and local similarity in the tower-layer over Nanjing area. *Boundary-Layer Meteorol* 82:1–21
- Yusup YB, Daud WRW, Zaharim A, Talib MZM (2008) Structure of the atmospheric surface layer over an industrialized equatorial area. *Atmospheric Res* 90:70–77

**Publisher's Note** Springer Nature remains neutral with regard to jurisdictional claims in published maps and institutional affiliations.